



Article

Long-Time Coherent Integration for the Spatial-Based Bistatic Radar Based on Dual-Scale Decomposition and Conditioned CPF

Suqi Li ¹, Yihan Wang ¹, Yanfeng Liang ² and Bailu Wang ^{1,*}

¹ School of Micro-Electronics and Communication Engineering, Chongqing University, Chongqing 401331, China; lisuqi@cqu.edu.cn (S.L.); wyhcqu@stu.cqu.edu.cn (Y.W.)

² China Academy of Electronics Information Technology, Beijing 100041, China; liangyanfeng@cetc.com.cn

* Correspondence: w_b_l3020@163.com or wangbailu@cqu.edu.cn

Abstract: This paper addresses the problem of weak maneuvering target detection in the space-based bistatic radar system through long-time coherent integration (LTCI). The space-based bistatic radar is vulnerable to the high-order range migration (RM) and Doppler frequency migration (DFM), since the target, the receiver and the transmitter all can play fast movement independently. To correct high-order RM and DFM, this usually involves joint high-dimensional parameter searching, incurring a large computational burden. In our previous work, a dual-scale (DS) decomposition of motion parameters was proposed, in which the optimal GRFT is conditionally decoupled into two cascade procedures called the modified generalized inverse Fourier transform (GIFT) and generalized Fourier transform (GFT), resulting in the DS-GRFT detector. However, even if the DS-GRFT detector preserves the superior performance and dramatically decreases the complexity, high-dimensional searching is still required. In this paper, by analyzing the structure of the DS-GRFT detector, we further designed a conditioned cubic phase function (CCPF) tailored to the range–slow-time signal after GIFT, breaking the joint high-dimensional searching into independent one-dimensional searching. Then, by connecting the proposed CCPF with the GIFT, we achieved a new LTCI detector called the DS-GIFT-CCPF detector, which obtained a significant computational cost reduction with acceptable performance loss, as demonstrated in numerical experiments.

Keywords: long-time coherent integration; space-based bistatic radar; high-order range migration; high-order Doppler frequency migration; generalized Radon–Fourier transform (GRFT); dual-scale decomposition



Citation: Li, S.; Wang, Y.; Liang, Y.; Wang, B. Long-Time Coherent Integration for the Spatial-Based Bistatic Radar Based on Dual-Scale Decomposition and Conditioned CPF. *Remote Sens.* **2024**, *16*, 1798. <https://doi.org/10.3390/rs16101798>

Academic Editors: Alin Achim, Shiyang Tang, Zhongyu Li, Hongyang An and Yan Wang

Received: 13 March 2024

Revised: 10 May 2024

Accepted: 16 May 2024

Published: 18 May 2024



Copyright: © 2024 by the authors. Licensee MDPI, Basel, Switzerland. This article is an open access article distributed under the terms and conditions of the Creative Commons Attribution (CC BY) license (<https://creativecommons.org/licenses/by/4.0/>).

1. Introduction

The bistatic radar [1–5] has many merits, such as destruction resistance and great anti-jamming and antistealth performance, taking advantage of the feature that its receiver does not emit any radiation, but capitalizes on the signals already emitted into the environment. A recent improvement of the bistatic radar is the space-based bistatic radar [2,5] which can provide wide coverage and long surveillance distance despite the curvature of the earth and airspace restrictions.

For radar early warning, an effective method is long-time coherent integration (LTCI). However, for maneuvering targets, energy defocusing, which means targets' energy is accumulated effectively, can occur due to range migration (RM) and Doppler frequency migration. Hence, to achieve stable detection performance, it is required to correct RM and DFM accurately. Different from the monostatic radar, the receiver of the bistatic radar is separated from the transmitter, thus the delay of the received signal not only depends on the relative movement of the target and the transmitter, but also on the relative movement of the target and the receiver. Especially for the space-based bistatic radar, in addition to the high maneuvering of targets, the transmitter and receiver also play a fast

motion, making the received signal even more complicated in the sense that the high-order RM and DFM, e.g., the cubic range curvature and the cubic DFM, become significant. As such, the demand for LTCI algorithms considering high-order RM and DFM correction is becoming increasingly prominent.

A type of feasible method is to correct the RM and DFM simultaneously. The representative method is the generalized Radon–Fourier transform (GRFT), which was introduced in [6] and proved to be an optimal detector based on multidimensional search procedures. The GRFT detector belongs to the Radon-based methods [7–11], which are one of the broadest families of LTCI methods. Although the GRFT method is considered to have theoretically optimal coherent accumulation and parameter estimation performance, its computational complexity is so huge that it is practically prohibitive. Another promising solution is the keystone transform matched filtering processing (KT-MFP) [12] method, in which KT is applied to eliminate RM caused by the baseband velocity, then MFP is performed to remove residual RM and DFM simultaneously. Additionally, the KT-MFP detector for maneuvering targets with second-order and first-order motion were described in [13,14], respectively. Later, in [15], the authors further observed that the MFP procedure in the KT-MFP detector has the same form as the GRFT detector in the frequency domain. The KT-MFP detector yields similar performance as the GRFT detector, but its computation burden is alleviated a lot. However, it still involves joint high-dimensional searching for high-order RM and DFM correction, i.e., joint searching of ambiguous velocity, acceleration, jerk, etc.

To avoid joint high-dimensional searching, several methods [5,16–18] have been proposed to correct RM and DFM in the way of cascade processing under some specific assumptions. In most cases, this kind of methods achieve improvements in computational efficiency, but have to compromise on detection performance. Specifically, under the assumption that the jerk motion will not lead to RM, ref. [16] first utilized the second-order KT (SKT) to eliminate RM caused by acceleration, then performed the Hough transform to detect the linear RM caused by the velocity. Nevertheless, this essentially belongs to noncoherent integration methods, hence it suffers from severe SNR loss because useful phase information is abandoned. What is more, the cubic range curvature could happen in cases of large jerk or high range resolution. In [5], it is assumed that the space-based bistatic radar emits a narrow-band chirp signal while the pulse repetition frequency is relative low; thus, both the third-order RM and linear RM caused by the baseband velocity are neglected. As a result, this method only needs to complete the quadratic range curvature and linear RM caused by blind velocity with the pre-estimation of the folding factor using the generalized SKT (GSKT). As for the DFM correction, this method utilizes the multiple product cubic phase function (MPCPF) method to estimate the target third-order motion parameters in independent one-dimensional search spaces, thus greatly improving computational efficiency. In [17,18], the authors proposed the adjacent cross correlation function (ACCF)-based LTCI method, which achieved cheap computational cost by reducing the order of DFM. However, the ACCF-based method is only suitable for the high-SNR case, due to the high-order nonlinear operation and the error propagation effect. To summarize, the performance degradation of the aforementioned methods arise from two aspects: one is the incomplete RM correction, and the other is the nonlinear transform used in the RM/DFM correction. Actually, it is really a tough task to balance the computational load and the detection performance.

Our previous analysis showed that, since RM and DFM share the same motion parameters, the RM and DFM correction procedures of most LTCI detection methods are coupled, referred to as the coupling effect of parameter search spaces. Affected by this effect, LTCI methods employed on the coupled parameter search space not only suffer from redundant computation, but also from lack of freedom in the sense that RM and DFM have to be jointly corrected. To this end, refs. [15,19] proposed a flexible dual-scale (DS) decomposition framework, based on which the standard GRFT family is factorized into a generalized inverse Fourier transform (GIFT) process in the range domain and GFT processes in the

Doppler domain conditioned on the coarse motion parameter, referred to as the DS-GRFT detector family, including DS-GRFT, second-order DS-KT-MFP, and third-order DS-KT-MFP algorithms. Compared to the standard GRFT detector family, the DS-GRFT detector family can provide comparable performance while providing significant improvement in computational efficiency. However, they still need joint high-dimensional searching on the fine parameter space when performing the DFM compensation, restricting its application in the spaced-based bistatic radar system.

Notably, the DS decomposition framework also provides another potential benefit which, due to the conditional decoupling of RM and DFM correction, is the possibility to adopt different algorithms in place of GIFT or GFT, considering practical requirements such as detection performance, computational efficiency, etc. Motivated by this, the LTCI algorithm of this paper is still formulated within the DS decomposition framework. The basic idea was to design a suitable CPF according to the characteristic of the range–slow-time signal after the GIFT, breaking the joint high-dimensional searching of the fine motion parameter space into independent one-dimensional searching. Specifically, the GIFT is first performed to complete the RM correction and a pre-compensation of DFM, and then, to correct the DFM caused by the fine motion parameters, the second-order and third-order motion parameters are estimated by resorting to the suitably designed conditioned CPF (CCPF), and finally, GFT is performed utilizing the estimated DFM compensation coefficients. As such, the resulting LTCI algorithm is called the DS-GIFT-CCPF detector. In general, the advantages of the proposed detector are two-fold:

- It inherits the advantage of the DS decomposition framework in that the RM can be fully corrected using the GIFT procedure on the coarse motion parameter space.
- It inherits the advantage of CPF such that joint three-dimensional searching is not required, but instead independent one-dimensional searching takes place.
- The proposed CCPF is designed in a much smaller space, i.e., the fine motion parameter space, conditioned on each coarse motion parameter. With this structure, multiple targets are grouped naturally according to coarse motion parameters, leading to an advantage of suppressing false peaks caused by cross-terms of the CPF.

Simulation results under the bistatic radar considering both single target and multiple targets highlight the performance of the proposed DS-GIFT-CCPF detector in terms of both superior detection ability and computational efficiency.

2. Background

2.1. Signal Model

We consider a T–R-type space-based bistatic radar for which the transmitter and the receiver are spatially separated. Particularly, in different applications, the transmitter and the receiver are placed on different types of platforms. We suppose that both the transmitter and the receiver can be put on an aircraft (including missile, satellite and so on), and a high-speed, high-maneuvering target is observed. Figure 1 shows the geometric relationship between the spaced-based bistatic radar system and the target, where the transmitter is located at point T and the receiver is located at point R ; the velocity vector of the transmitter and the receiver are denoted by \vec{v}_T and \vec{v}_R , respectively, while the acceleration vector of the transmitter and the receiver are denoted by \vec{a}_T and \vec{a}_R , respectively; the target is at P initially, and the velocity vector and the acceleration vector are denoted by \vec{v} and \vec{a} , respectively; the vector from the transmitter and the receiver to the point P are denoted as \vec{R}_{Tp} and \vec{R}_{Rp} , respectively. When the target is moving, both \vec{R}_{Tp} and \vec{R}_{Rp} change with time. At the initial time, \vec{R}_{Tp} and \vec{R}_{Rp} are denoted as \vec{R}_{Tp0} and \vec{R}_{Rp0} .

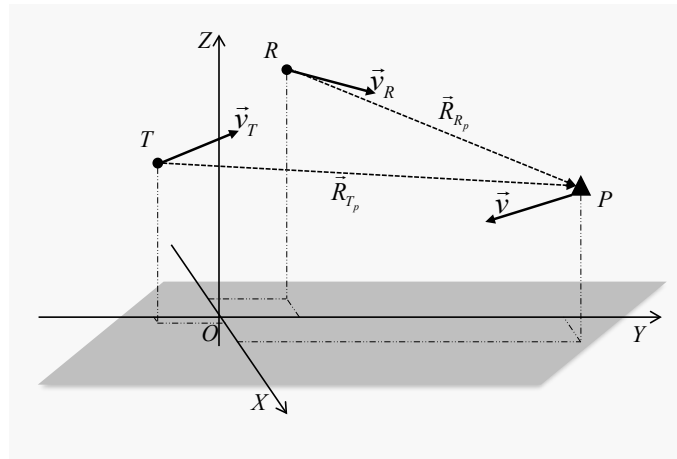


Figure 1. Geometric relationship between the spaced-based bistatic radar system and the target.

We suppose that the PC is performed in the frequency domain. According to the stationary phase principle [20], after the received baseband signal is multiplied by the reference signal in the range frequency-pulse domain, the signal model can be expressed as

$$y(f_k, t_m) = A_1 \exp \left[-j \frac{2\pi}{c} (f_k + f_c) R(t_m) \right] + w(f_k, t_m) \quad (1)$$

where A_1 denotes the target complex attenuation in the frequency domain; t_m is the slow time (inter-pulse sampling time), satisfying $t_m = m \cdot \text{PRT}$ for $m = 1, \dots, M$, with M being the number of pulses; PRT is the pulse repetition time and its corresponding pulse repetition frequency (PRF) is $\text{PRF} = \frac{1}{\text{PRT}}$; f_c is the carrier frequency; c is the velocity of light, i.e., $c = 3 \times 10^8$ m/s; $w(f_k, t_m)$ is the Gaussian-distributed noise in the frequency domain with zero-mean and variance σ^2 ; $R(t_m)$ is the instantaneous slant range between the receiver and the transmitter. It should be noted that the noise $w(f_k, t_m)$ is omitted for easy analysis hereafter.

Combining the geometric relationship given in Figure 1, $R(t_m)$ can be computed by [3]:

$$R(t_m) = c_0 + c_1 t_m + c_2 t_m^2 + c_3 t_m^3 \quad (2)$$

where c_0 denotes the slant range from the transmitter to the receiver at $t_m = 0$; $[c_1, c_2, c_3]$ represents the vector consisting of the radial components of, respectively, target initial velocity, acceleration and jerk, i.e.,

$$c_0 = R_{T_{p0}} + R_{R_{p0}}, c_1 = v_{T_p} + v_{R_p}, \quad (3)$$

$$c_2 = \frac{a_{T_p} + a_{R_p}}{2} + \frac{(\vec{v} - \vec{v}_T)^2 - v_{T_p}^2}{2R_{T_{p0}}} + \frac{(\vec{v} - \vec{v}_R)^2 - v_{R_p}^2}{2R_{R_{p0}}}, \quad (4)$$

$$c_3 = \frac{(\vec{a} - \vec{a}_T) \cdot (\vec{v} - \vec{v}_T) - a_{T_p} v_{T_p}}{2R_{T_{p0}}} + \frac{(\vec{a} - \vec{a}_R) \cdot (\vec{v} - \vec{v}_R) - a_{R_p} v_{R_p}}{2R_{R_{p0}}} + \quad (5)$$

$$\frac{v_{T_p}^3 - v_{T_p} (\vec{v} - \vec{v}_T)^2}{2R_{T_{p0}}^2} + \frac{v_{R_p}^3 - v_{R_p} (\vec{v} - \vec{v}_R)^2}{2R_{R_{p0}}^2}$$

with

$$v_{T_p} = \vec{R}_{T_{p0}}(\vec{v} - \vec{v}_T)/R_{T_{p0}} \quad (6)$$

$$v_{R_p} = \vec{R}_{R_{p0}}(\vec{v} - \vec{v}_R)/R_{R_{p0}} \quad (7)$$

$$a_{T_p} = \vec{R}_{T_{p0}}(\vec{a} - \vec{a}_T)/R_{T_{p0}} \quad (8)$$

$$a_{R_p} = \vec{R}_{R_{p0}}(\vec{a} - \vec{a}_R)/R_{R_{p0}} \quad (9)$$

and $R_{T_{p0}}$ and $R_{R_{p0}}$ denote the initial distance between the transmitter T and the receiver R to the target P , respectively.

Then, we perform IFFT on the range dimension for the signal in (1); we have

$$y(\tau_n, t_m) = A_2 \text{asinc}[B_r(\tau_n - R(t_m)/c)] \exp\{-j\pi B_r(\tau_n - R(t_m)/c)\} \exp\left\{-j\frac{2\pi}{\lambda}R(t_m)\right\}, \quad (10)$$

where: A_2 denotes the target complex attenuation in the time domain; τ_n the fast time (intra-pulse sampling time), which is a multiple of the sampling interval T_s , i.e., $\tau_n = nT_s$ and $T_s = 1/f_s$; λ is the wave length, i.e., $\lambda = c/f_c$; $\text{asinc}(\cdot)$ is the aliased sinc (asinc) function [21,22] (also called Dirichlet [23] or periodic sinc function), i.e.,

$$\text{asinc}(B_r\tau_n) = \frac{\sin(\pi B_r\tau_n)}{K_{\text{valid}} \sin(\pi\Delta f\tau_n)}, \quad (11)$$

with Δf being the interval of frequency bins, K_{valid} the valid number of frequency bins and B_r the signal bandwidth, i.e., $B_r = K_{\text{valid}} \Delta f$.

2.2. RM and DFM Effects

Substituting (2) into (10) yields

$$y(\tau_n, t_m) = A'_2 \exp\left\{-j\pi B_r\left(\tau_n - (c_0 + \sum_{p=1}^3 c_p t_m^p)/c\right)\right\} \times \exp\left\{-j\frac{2\pi}{\lambda}\left(c_1 + \sum_{p=2}^3 c_p t_m^p\right)\right\} \text{asinc}[B_r(\tau_n - (c_0 + \sum_{p=1}^3 c_p t_m^p)/c)], \quad (12)$$

where $A'_2 = A_2 \exp\left\{-j\frac{2\pi c_0}{\lambda}\right\}$.

It is seen from (12) that the terms $c_p t_m^p/c$ ($p = 1, \dots, 3$) may result in the RM effect. Specifically, the t_m -, t_m^2 - and t_m^3 - terms may cause linear range walk and quadratic range curvature, cubic range curvature and high-order DFM, respectively. Additionally, each term $c_p t_m^p/\lambda$ ($p \geq 2$) may lead to p -order DFM. Both RM and DFM effects are major factors leading to target energy dispersion if the corresponding motion parameters are not effectively compensated.

3. Dual-Scale GIFT-CCPF Detector

In this paper, we followed the DS decomposition framework [15,19] to study weak maneuvering target detection for the bistatic radar. In this section, we first provide the DS decomposition of motion parameters for the bistatic radar, on the basis of which the DS-GRFT detector (considered to be equivalent to the optimal GRFT detector [6]) is reviewed briefly for subsequent development. As we analyze later, even if the overall computational burden has been largely reduced utilizing the DS decomposition, high-dimensional joint searching (on the fine parameter space) is still required, especially when the DFM caused by the high-order motion parameters cannot be neglected in the bistatic radar. On the other hand, the CPF [5,24–27] has been proved to be an effective method to decrease the dimension of parameter searching, but has an acceptable performance. Inspired by this, a new LTCI method is proposed by combining the GIFT and a suitably designed conditioned CPF in the DS decomposition framework in this section.

3.1. Dual-Scale Decomposition of Motion Parameters for the Bistatics Radar

For the purpose of decoupling motion parameters and enhancing the flexibility of RM and DFM compensation, a DS decomposition of the motion parameters was proposed in [15]. This paper further provides the counterpart of the bistatic radar as follows:

$$\tilde{c}_p = \tilde{c}_{p,c} + \tilde{c}_{p,f}, \quad p = 1, 2, 3. \quad (13)$$

where $\tilde{c}_{p,c}$ is the coarse motion parameter of \tilde{c}_p corresponding to the RM correction and $\tilde{c}_{p,f}$ is the residual part of c_p , called the fine motion parameter, corresponding to the DFM correction.

According to (49), in [15], to avoid RM, the coarse motion parameter should be set as

$$\tilde{c}_{p,c} = \text{round}\left(\frac{c_p - c_{p,\min}}{\Delta c_{p,c}}\right) \Delta c_{p,c} + c_{p,\min}, \quad (14)$$

where $\Delta c_{p,c} = \Delta_{\text{RM},p}$, i.e.,

$$\Delta_{\text{RM},p} \triangleq \alpha_p c / (f_s T^p), \quad p = 1, 2, 3. \quad (15)$$

with $0 \leq \alpha_p \leq 1$, $p = 1, 2, 3$, satisfying $\sum_{p=1}^3 \alpha_p = 1$.

On the other hand, according to (50), in [15], to avoid DFM, the fine motion parameter should be set as

$$\tilde{c}_{p,f} = \text{round}\left(\frac{c_p - \tilde{c}_{p,c} + \Delta c_{p,c}/2}{\Delta c_{p,f}}\right) \Delta c_{p,f} - \frac{\Delta c_{p,c}}{2}, \quad (16)$$

where $\Delta c_{p,f} = \Delta_{\text{DFM},p}$, i.e.,

$$\Delta_{\text{DFM},p} \triangleq \alpha_p c / (f_c T^p), \quad p = 1, 2, 3. \quad (17)$$

Correspondingly, the search spaces of the coarse part of target motion parameters are defined as

$$\mathbb{C}_{p,c} \triangleq [c_{p,\min} : \Delta c_{p,c} : c_{p,\max}], \quad p = 1, 2, 3. \quad (18)$$

while the search spaces $\mathbb{C}_{p,f}$ of the fine part are defined as

$$\mathbb{C}_{p,f} \triangleq [-\Delta c_{p,c}/2 : \Delta c_{p,f} : \Delta c_{p,c}/2], \quad p = 1, 2, 3. \quad (19)$$

3.2. Dual-Scale GRFT Detector for the Bistatics Radar

According [15], under the condition $\frac{f_c/f_s}{M} \leq 1$, by utilizing the dual-scale decomposition (13), the range Doppler joint GRFT can be factorized into a GIFT process in the range domain and GFT processes in the Doppler domain conditioned on the coarse motion parameter. As such, the joint correction of RM and DFM effects is decoupled into a cascade procedure, i.e.,

$$\text{GRFT}_{y(f_k, t_m)}(\tilde{\mathbf{c}}) \approx \text{GFT}_{m\text{GIFT}_{y(f_k, t_m)}(\tilde{\mathbf{c}}_c)}(\tilde{\mathbf{c}}'_f), \quad (20)$$

where: $\tilde{\mathbf{c}} = [\tilde{c}_0, \tilde{c}_1, \dots, \tilde{c}_p]$; $\tilde{\mathbf{c}}_c = [\tilde{c}_0, \tilde{c}_{1,c}, \dots, \tilde{c}_{p,c}]$; $\tilde{\mathbf{c}}_f = [\tilde{c}_{1,f}, \dots, \tilde{c}_{p,f}]$; $\tilde{\mathbf{c}}'_f = [\kappa \tilde{c}_{1,f}, \dots, \kappa \tilde{c}_{p,f}]$; $\kappa \triangleq 1 - \frac{B_r}{2f_c}$; $m\text{GIFT}$ and GFT denote the generalized IFFT and FFT operations [15], respectively, i.e.,

$$\begin{aligned} m\text{GIFT}_{y(f_k, t_m)}(\tilde{\mathbf{c}}_c) &\triangleq \sum_{k=1}^K y(f_k, t_m) \overline{H}_{\text{RM}}(f_k, t_m; \tilde{\mathbf{c}}_c) \exp\left[j \frac{2\pi}{c} f_k \tilde{c}_0\right] \\ &= \text{IFFT}\{y(f_k, t_m) \overline{H}_{\text{RM}}(f_k, t_m; \tilde{\mathbf{c}}_c)\} H_{\text{pre-DFM}}(t_m; \tilde{\mathbf{c}}_c), \end{aligned} \quad (21)$$

$$\begin{aligned} \text{GFT}_{y(\tau_n, t_m; \tilde{\mathbf{c}}_c)}(\tilde{\mathbf{c}}'_f) &\triangleq \sum_{p=1}^P y(\tau_n, t_m; \tilde{\mathbf{c}}_c) \bar{H}_{\text{DFM}}(t_m; \tilde{\mathbf{c}}'_f) \exp \left[j \frac{2\pi}{\lambda} \tilde{c}'_{1,f} t_m \right] \\ &= \text{FFT} \left\{ y(\tau_n, t_m; \tilde{\mathbf{c}}_c) \bar{H}_{\text{DFM}}(t_m; \tilde{\mathbf{c}}'_f) \right\} \end{aligned} \quad (22)$$

with

$$\bar{H}_{\text{RM}}(f_k, t_m; \tilde{\mathbf{c}}_c) \triangleq \exp \left[j \frac{2\pi}{c} f_k \left(\sum_{p=1}^P \tilde{c}_{p,c} t_m^p \right) \right], \quad (23)$$

$$H_{\text{pre-DFM}}(t_m; \tilde{\mathbf{c}}_c) \triangleq \exp \left[j \frac{2\pi}{\lambda} \sum_{p=1}^P \tilde{c}_{p,c} t_m^p \right], \quad (24)$$

$$\bar{H}_{\text{DFM}}(t_m; \tilde{\mathbf{c}}'_f) \triangleq \exp \left[j \frac{2\pi}{\lambda} \left(\sum_{p=2}^P \tilde{c}'_{p,f} t_m^p \right) \right]. \quad (25)$$

Let $y(\tau_n, t_m; \tilde{\mathbf{c}}_c)$ denote the range–slow time signals after RM correction by mGIFT on coarse search space, i.e.,

$$y(\tau_n, t_m; \tilde{\mathbf{c}}_c) = \text{mGIFT}_{y(f_k, t_m)}(\tilde{\mathbf{c}}_c). \quad (26)$$

When $|\tilde{\mathbf{c}}_c - \mathbf{c}_c| \rightarrow 0$, (26) yields

$$y(\tau_n, t_m; \tilde{\mathbf{c}}_c) = A_3 \exp \left[-j \frac{2\pi}{\lambda} (c'_{1,f} t_m + c'_{2,f} t_m^2 + c'_{3,f} t_m^3) \right], \quad (27)$$

where $A_3 \triangleq A'_2 \exp\{-j\pi B_r(\tau_n - c_0/c)\}$.

According to the cascade procedure of the DS-GRFT detector, the following DFM correction on the fine search space is given by

$$|\text{GFT}_{y(\tau_n, t_m; \tilde{\mathbf{c}}_c)}(\tilde{\mathbf{c}}_f)| \underset{H_1}{\overset{H_0}{\gtrless}} \gamma_{\text{LRT}}, \quad \tilde{\mathbf{c}}_f \in \mathbb{C}_f, \quad (28)$$

where: γ_{LRT} is a suitable threshold and $\mathbb{C}_f = \mathbb{C}_{1,f} \times \mathbb{C}_{2,f} \times \mathbb{C}_{3,f}$. Observing (28), this DFM procedure still involves three-dimensional searching, having cubical computational complexity with respect to the size of fine parameter space, which is still generally not cheap in practice.

3.3. Conditional CPF

The idea of this paper is to reduce the dimension of parameter searching for the DFM correction procedure in (28) by means of the CPF-based transformation [5,24–27]. As we mentioned in the Introduction, the existing LTCI detectors utilizing the CPF [5] mainly assume that a part of motion parameters will not lead to RM, i.e., second or third motion parameters. However, in the application of the bistatic radar, if the RM caused by the second and third motion parameters is neglected, the energy loss may exist after integration, decreasing the estimation accuracy of the MPCPF. To avoid this problem, in this paper, we constructed a conditioned CPF (CCPF) to estimate the fine acceleration $c_{2,f}$ and jerk $c_{3,f}$ of the target (conditioned on each coarse motion parameter) through two rounds of one-dimensional searches on the constructed parameter space. Notably, two rounds of searching were adopted to obtain respective unique solutions for the acceleration and jerk parameters. Then, the GFT, considering the DFM compensation function using the estimated acceleration and jerk parameters, was applied to decide all the final estimates of the coarse and fine motion parameters.

According to (20) and (21), the mGIFT completes the RM correction with the compensation coefficient $\bar{H}_{\text{RM}}(f_k, t_m; \tilde{\mathbf{c}}_c)$. Furthermore, the mGIFT also includes a pre-compensation for the DFM with respect to the coarse motion parameter, i.e., $H_{\text{pre-DFM}}(t_m; \tilde{\mathbf{c}}_c)$. As such,

after the mGIFT, we achieve the range–slow-time signals conditioned on each given coarse motion parameter \tilde{c}_c , i.e., $y(\tau_n, t_m; \tilde{c}_c)$.

Borrowing the idea of [5], we constructed a CPF with the conditioned signal $y(\tau_n, t_m; \tilde{c}_c)$ called the CCPF, i.e.,

$$\begin{aligned} \text{CCPF}_{y(\tau_n, t_m; \tilde{c}_c)}(t_\rho; \Omega) &= \sum_{i=1}^{M/2} y(\tau_n, t_\rho + t_i; \tilde{c}_c) y(\tau_n, t_\rho - t_i; \tilde{c}_c) \\ &\times y^*(\tau_n, t_\rho; \tilde{c}_c) y^*(\tau_n, t_\rho; \tilde{c}_c) \exp \left[j \frac{2\pi}{\lambda} \Omega t_i^2 \right], \end{aligned} \quad (29)$$

where $t_i = i \cdot PRT$; $\rho = M/2$ and Ω denotes the constructed instantaneous frequency rate. Then, we obtained the peak position for Ω according to the following maximization:

$$\hat{\Omega} = \arg \max_{\Omega \in \mathbb{C}_\Omega} |\text{CCPF}_{y(\tau_n, t_m; \tilde{c}_c)}(t_\rho; \Omega)|, \quad (30)$$

where \mathbb{C}_Ω denotes the search space of Ω .

Substituting the specific expression after mGIFT (27) into (29) and re-arranging yields

$$\text{CCPF}_{y(\tau_n, t_m; \tilde{c}_c)}(t_\rho; \Omega) = \sum_{i=1}^{M/2} \exp \left[j \frac{2\pi}{\lambda} (\Omega - 2c'_{2,f} - 6c'_{3,f} t_\rho) t_i^2 \right]. \quad (31)$$

Accordingly, the peak of the above function is located at

$$\hat{\Omega} = 2c'_{2,f} + 6c'_{3,f} t_\rho. \quad (32)$$

It is worthy noting that, due to the DS decomposition, the fine motion parameters $c'_{p,f}$, $p = 2, 3$ have been limited to a small region $\mathbb{C}'_{p,f} = [-\kappa \Delta_{p,c}/2, \kappa \Delta_{p,c}/2]$. Accordingly, the search space of \mathbb{C}_Ω can be constructed by

$$\mathbb{C}_\Omega = \{ \Omega = 2c'_{2,f} + 6c'_{3,f} t_\rho : (c'_{2,f}, c'_{3,f}) \in \kappa^2 \mathbb{C}_{2,f} \times \mathbb{C}_{3,f} \}. \quad (33)$$

Clearly, \mathbb{C}_Ω given in (33) is not a heterogeneous search space. To traverse \mathbb{C}_Ω , it is required to search the two-dimensional space $\mathbb{C}_{2,f} \times \mathbb{C}_{3,f}$. As such, the original three-dimensional searching problem on \mathbb{C}_f is reduced to a two-dimensional searching problem on space $\mathbb{C}_{2,f} \times \mathbb{C}_{3,f}$.

What is more, it is possible to further exploit dimension reduction of the search space by homogenizing the space \mathbb{C}_Ω . Specifically, we first determine the scope of the space $\overline{\mathbb{C}}_\Omega$, and then discretize this scope by a uniform step size $\Delta\Omega$, i.e.,

$$\overline{\mathbb{C}}_\Omega = [-(2\Delta c_{2,c} + 6\Delta c_{3,c} t_\rho)\kappa/2 : \Delta\Omega : (2\Delta c_{2,c} + 6\Delta c_{3,c} t_\rho)\kappa/2]. \quad (34)$$

In this way, the two-dimensional searching problem can be further reduced to two instances of one-dimensional searching problems. However, since the homogeneous space $\overline{\mathbb{C}}_\Omega$ is different from \mathbb{C}_Ω , it may lead to estimation deviation for $c_{2,f}$ and $c_{3,f}$, resulting in performance loss. Even if searching with a sufficiently small step size $\Delta\Omega$ can alleviate this problem, the computational burden will increase accordingly. Our experiment result suggests that when the size of $\overline{\mathbb{C}}_\Omega$ is comparable with the size of the fine motion parameters, i.e., $|\overline{\mathbb{C}}_\Omega| = \frac{f_c}{f_s}$, the performance loss caused by homogenizing the search space can be controlled within 1 dB at $P_d = 0.9$. A such, $\Delta\Omega = \frac{(2\Delta c_{2,c} + 6\Delta c_{3,c} t_\rho)\kappa f_s}{f_c}$ can be a preferable choice to balance the detection performance and computational burden in practice.

3.4. The Single-Target Case

It is easy to check that there are multiple pairs of $[c'_{2,f}, c'_{3,f}]$ that can satisfy (32), but all pairs of solutions are on the straight line determined by the following equation:

$$2c'_{2,f} + 6c'_{3,f}t_\rho - \hat{\Omega} = 0. \quad (35)$$

with the slope being $-6t_\rho$.

As a matter of fact, two straight lines with different slopes can confirm the unique solution. Hence, given two time positions t_{ρ_1} and t_{ρ_2} satisfying $\rho_1 \neq \rho_2$, we can construct the following equation:

$$\hat{\Omega} = \mathbf{X}\hat{c}'_f \quad (36)$$

where

$$\hat{\Omega} \triangleq [\hat{\Omega}_1, \hat{\Omega}_2]^T, \quad (37)$$

$$\hat{c}'_f \triangleq [c'_{2,f}, c'_{3,f}]^T, \quad (38)$$

$$\mathbf{X} \triangleq \begin{bmatrix} 2 & 6t_{\rho_1} \\ 2 & 6t_{\rho_2} \end{bmatrix}. \quad (39)$$

Notably, $\hat{\Omega}_1$ and $\hat{\Omega}_2$ are estimated by finding the peaks of the CCPFs at two different time positions ρ_1 and ρ_2 , respectively, according to (30). Two different time positions can ensure the invertibility of the matrix \mathbf{X} , and, thus, ensure the unique estimate of \hat{c}'_f , i.e.,

$$\hat{c}'_f = \kappa \hat{c}_f = \mathbf{X}^{-1}\hat{\Omega}, \quad (40)$$

where $\hat{c}'_f = [c'_{2,f}, c'_{3,f}]^T$; $\hat{c}_f = [\hat{c}_{2,f}, \hat{c}_{3,f}]^T$, $\hat{c}_{2,f}$ and $\hat{c}_{3,f}$ are estimates of $c_{2,f}$ and $c_{3,f}$, conditioned on the coarse parameter.

Remark 1. Considering that the choice of the two different time positions ρ_1 and ρ_2 affects the variance of the motion parameter estimates, we follow the suggested default setting for the two time positions. Specifically, the first time position ρ_1 chooses $(M+1)/2$, guaranteeing that $\hat{c}_{2,f}$ are asymptotically optimal at high SNR, while the second time position ρ_2 chooses $0.65M + 0.5$ [24], giving rise to a minimum asymptotic mean-square error for $\hat{c}_{3,f}$ at high SNR.

According to the aforementioned procedure, to estimate the motion parameters $c_{2,f}$ and $c_{3,f}$, we only need two instances of one-dimensional searches on space $\bar{\mathbb{C}}_\Omega$ (getting $\hat{\Omega}_1$ and $\hat{\Omega}_2$, respectively). Indeed, the size of $\bar{\mathbb{C}}_\Omega$ is comparable with $\mathbb{C}_{2,f}$ or $\mathbb{C}_{3,f}$. Then, the DFM matching coefficients can be constructed by estimates $\hat{c}_{2,f}$ and $\hat{c}_{3,f}$, i.e.,

$$\bar{H}_{\text{DFM}}(t_m; \hat{c}_{2,f}, \hat{c}_{3,f}) = \exp \left[j \frac{2\pi}{\lambda} \kappa (\hat{c}_{2,f} t_m^2 + \hat{c}_{3,f} t_m^3) \right]. \quad (41)$$

Then, following the framework of the DS-GRFT, as long as the condition $\frac{f_c/f_s}{M} \leq 1$ is satisfied, the DFM correction procedure can be simplified by applying (41) as follows:

$$|\text{GFT}_{y_{\text{GIFT}}(\tau_n, t_m; \tilde{\mathbf{c}}_c)}(\tilde{\mathbf{c}}'_f)| = \left| \text{FFT} \left\{ y(\tau_n, t_m; \tilde{\mathbf{c}}_c) \bar{H}_{\text{DFM}}(t_m; \hat{c}_{2,f}, \hat{c}_{3,f}) \right\} \right| \stackrel{H_0}{\leq} \gamma_{\text{LRT}}, \tilde{c}'_{1,f} \in \kappa \mathbb{C}_{1,f}, \quad (42)$$

where $\tilde{\mathbf{c}}'_f = [\tilde{c}'_{1,f}, \hat{c}_{2,f}, \hat{c}_{3,f}]$. On the condition that $\hat{c}_{2,f}$ and $\hat{c}_{3,f}$ have been achieved, it only requires one instance of a one-dimensional search on the space $\mathbb{C}_{1,f}$ to complete (42).

3.5. The Multi-Target Case

It is worthy noting that multiple targets has been divided into groups naturally utilizing the DS decomposition, and, inside each group, the targets share the same coarse motion parameters. For targets falling into different range bins or having different coarse motion parameters, the CPF is performed independently, thus avoiding cross-term among these targets. If multiple targets fall into the same range bin and have the same coarse motion parameter, it can happen that multiple peaks are found for the CCPF (32), resulting in multiple estimates conditioned on the given coarse motion parameters. It should be noted that this case is not common, but can happen for group target or swarm targets in which targets share similar kinematic characteristic. Similar to the single-target case, to achieve unique solutions of fine motion parameter estimates, the maximization (32) is performed twice for two different time positions t_{ρ_1} and t_{ρ_2} , yielding two groups of estimates, respectively,

$$\begin{aligned}\Omega_1 &= [\Omega_1^{(1)}, \Omega_1^{(2)}, \dots, \Omega_1^{(n_1)}] \\ \Omega_2 &= [\Omega_2^{(1)}, \Omega_2^{(2)}, \dots, \Omega_2^{(n_2)}]\end{aligned}\quad (43)$$

Without loss of generality, we assume $n_1 \geq n_2$ hereafter.

Clearly, the association relationship (with respect to the same target) between elements of Ω_1 and those of Ω_2 is unknown and thus needs to be estimated first. To this end, we model the association map as an injective function $\theta: \{1, \dots, n_1\} \rightarrow \{1, \dots, n_2\}$ such that $\theta(i) = \theta(i') > 0$ implies $i = i'$. Let $\hat{\mathbf{c}}_f^{(i,\theta)} = [\kappa \hat{c}_{2,f}^{(i,\theta)}, \kappa \hat{c}_{3,f}^{(i,\theta)}]$ denote unique solutions of fine motion parameters solved by $(\Omega_1^{(i)}, \Omega_2^{(\theta(i))})$, $i = 1, \dots, n_1$ utilizing (40). The corresponding DFM matching coefficients are then constructed utilizing $\hat{\mathbf{c}}_f^{(i,\theta)}$ as follows:

$$\bar{H}_{\text{DFM}}(t_m; \hat{c}_{2,f}^{(i,\theta)}, \hat{c}_{3,f}^{(i,\theta)}) = \exp \left[j \frac{2\pi}{\lambda} \kappa \left(\hat{c}_{2,f}^{(i,\theta)} t_m^2 + \hat{c}_{3,f}^{(i,\theta)} t_m^3 \right) \right]. \quad (44)$$

Accordingly, the accumulated energy after the DFM correction using (44) is as follows:

$$E^{(i,\theta(i))} = \max_{\tilde{\mathbf{c}}_{1,f} \in \mathbb{C}_{1,f}} \left| \text{FFT} \left\{ y(\tau_n, t_m; \mathbf{c}_c) \bar{H}_{\text{DFM}}(t_m; \hat{c}_{2,f}^{(i,\theta)}, \hat{c}_{3,f}^{(i,\theta)}) \right\} \right|. \quad (45)$$

It is clear that the higher the accumulated energy $E^{(i,\theta(i))}$, the larger probability that fine motion parameters $[\hat{c}_{2,f}^{(i,\theta)}, \hat{c}_{3,f}^{(i,\theta)}]$ are correctly estimated. What is more, assuming that the noise is white and Gaussian, and given the false alarm probability P_{FA} , the accumulated energy of the target under correct estimation should satisfy

$$E^{(i,\theta(i))} > \gamma_{\text{LRT}}, \quad (46)$$

where $\gamma_{\text{LRT}} = \sqrt{-M K \sigma^2 \ln P_{\text{FA}}}$. In addition, taking advantage of the DS decomposition, another constraint condition also can be utilized, namely, the solved fine parameters $\hat{c}_{2,f}^{(i,\theta)}$ and $\hat{c}_{3,f}^{(i,\theta)}$ are within their corresponding scope $\mathbb{C}_{2,f}$ and $\mathbb{C}_{3,f}$, respectively.

Considering both aforementioned aspects, we construct the cost function of the matching pair (i, j) , i.e.,

$$\mathcal{C}(i, j) = \begin{cases} \frac{E^{(i,j)}}{\gamma_{\text{LRT}}}, & \hat{c}_{p,f} \in \mathbb{C}_{p,f}, \forall p = 2, 3, (i, j) \in [1, n_1] \times [1, n_2]. \\ 1, & \text{otherwise} \end{cases} \quad (47)$$

Finally, the global cost function considering all targets is constructed by

$$\mathcal{C}^{(\theta)} = - \sum_{i=1}^{n_1} \ln(\mathcal{C}(i, \theta(i))), \quad (48)$$

then, the “best” association map is obtained by the following maximization:

$$\hat{\theta} = \underset{\theta}{\operatorname{argmax}} C^{(\theta)}. \quad (49)$$

Remark 2. This optimization problem can be modeled by a linear assignment problem solved by the Hungarian algorithm with computational complexity $\mathcal{O}(n_1^3)$ [28]. Considering that the CCPF is performed under each given coarse motion parameter, this optimization finding the best association map needs to be solved only when multiple targets fall into the same range bin and have the same coarse motion parameter. Hence, n_1 is generally a small number; hence, the computational burden to solve this optimization could be small in practice.

Finally, after the “best” association map is achieved, to get the final motion parameter estimations, the procedure (50) is performed again for each $i = 1, \dots, n_1$ and $\tilde{\mathbf{c}}_c \in \mathbb{C}_c$, i.e.,

$$|\operatorname{GFT}_{y_{\operatorname{GIFT}(\tau_n, t_m; \tilde{\mathbf{c}}_c)}}(\tilde{\mathbf{c}}'_f)| = \left| \operatorname{FFT} \left\{ y(\tau_n, t_m; \tilde{\mathbf{c}}_c) \bar{H}_{\operatorname{DFM}}(t_m; \hat{c}_{2,f}^{(i,\hat{\theta})}, \hat{c}_{3,f}^{(i,\hat{\theta})}) \right\} \right| \underset{H_1}{\overset{H_0}{\lesseqgtr}} \gamma_{\operatorname{LRT}}, \tilde{\mathbf{c}}'_{1,f} \in \kappa \mathbb{C}_{1,f}. \quad (50)$$

3.6. Summary

To summarize, the proposed method works as follows: applying the DS decomposition of motion parameters, first, the mGIFT (21) is performed on the coarse motion parameter space \mathbb{C}_c for the RM compensation and a pre-compensation of DFM; a suitable designed CCPF is then constructed applying (31) to estimate the fine part of high-order motion parameters conditioned on the coarse motion parameters, on the basis of which the GFT is finally used as the detection statistic to estimate the all the motion parameters. As such, the resulting LTCI algorithm is called the DS-GIFT-CCPF detector.

Compared to the DS-GRFT procedure, the computation load of the proposed DS-GIFT-CCPF detector is decreased significantly, in the sense that the three-dimensional joint search in the fine parameter space is reduced to three instances of one-dimensional independent searches. The detailed computation complexity analysis is shown in the following subsection. On the other hand, compared to existing MPCPF-based detectors, the energy accumulation performance of the proposed DS-GIFT-CCPF detector is much better from the view that the RM is fully corrected by the GIFT, taking advantage of DS correction framework. Nevertheless, due to the nonlinear operations of the CCPF, the detector performance of the proposed DS-GIFT-CCPF detector decreases a bit compared with the DS-GRFT detector.

Let $\hat{\mathbf{c}}_c = \{\hat{c}_0, \dots, \hat{c}_{p,c}\}$ and $\hat{\mathbf{c}}'_f = \{\kappa \hat{c}_{1,f}, \dots, \kappa \hat{c}_{p,f}\}$ denote the parameter estimates of a moving target's motion with the cascade correction procedure of RM and DFM in (50). Then, after RM and DFM compensations with estimated motion parameters, the target can be finely focused in the fast-time range and slow-time Doppler domain, i.e.,

$$\begin{aligned} & \operatorname{GFT}_{m\operatorname{GIFT}_{y(f_k, t_m)}(\hat{\mathbf{c}}_c)}(\hat{\mathbf{c}}'_f) \\ &= A_4(\tau_n) \operatorname{asinc} \left\{ B \left(\tau_n(\hat{c}_0) - \frac{c_0}{c} \right) \right\} \operatorname{asinc} \left\{ \operatorname{PRF} \left(\hat{f}_d(\hat{c}'_{1,f}) - \frac{c'_{1,f}}{\lambda} \right) \right\} \end{aligned} \quad (51)$$

where $A_4(\tau_n)$ denotes the target complex attenuation after GIFT and GFT, and $\hat{f}_d(\hat{c}'_{1,f})$ the Doppler frequency estimate, i.e., $\hat{f}_d(\hat{c}'_{1,f}) = \frac{c'_{1,f}}{\lambda}$.

4. Implementation Issues

4.1. Pseudo-Code of the Proposed DS-GIFT-CCPF Detector

This subsection provides pseudo-code of the proposed DS-GIFT-CCPF detector. The DS-GIFT-CCPF involves two cascade procedures, i.e., GIFT compensation with respect to the coarse motion parameters followed by CCPF compensation with respect to the fine

motion parameters. Hence, we first provide pseudo-code of CCPF operation, in Algorithm 1. One can refer to [15] for pseudo-codes of GIFT and GFT operations. Then, pseudo-code of the DS-GIFT-CCPF is given in Algorithm 2.

Algorithm 1: CCPF

INPUT: $y(\tau_n, t_m; \tilde{\mathbf{c}}_c)$ of the form (26) and a given $\tilde{\mathbf{c}}_c$;
OUTPUT: motion parameter estimates $\hat{\mathbf{c}}'_f = [c'_{2,f}, c'_{3,f}]^T$;
Initialize $\rho_1 = M/2, \rho_2 = M/2 + \text{floor}(0.11M), M' = M - \rho_2$;
function CCPF ($y(\tau_n, t_m; \tilde{\mathbf{c}}_c)$)
for $i = 1, 2$ **do**
 $\bar{\mathbb{C}}_{\Omega_i} = [-(2\Delta c_{2,c} + 6\Delta c_{3,c} t_{\rho_i})\kappa/2 : \Delta\Omega : (2\Delta c_{2,c} + 6\Delta c_{3,c} t_{\rho_i})\kappa/2]$;
 for $\Omega \in \bar{\mathbb{C}}_{\Omega_i}$ **do**
 $\text{CCPF}_{y(\tau_n, t_m; \tilde{\mathbf{c}}_c)}(t_{\rho_i}; \Omega_i) =$
 $\sum_{i=1}^{M'} y(\tau_n, t_{\rho_i} + t_i; \tilde{\mathbf{c}}_c) y(\tau_n, t_{\rho_i} - t_i; \tilde{\mathbf{c}}_c) y^*(\tau_n, t_{\rho_i}; \tilde{\mathbf{c}}_c) y^*(\tau_n, t_{\rho_i}; \tilde{\mathbf{c}}_c) \exp[j\frac{2\pi}{\lambda}\Omega_i t_i^2]$;
 end
 $\hat{\Omega}_i = \arg \max_{\Omega \in \bar{\mathbb{C}}_{\Omega_i}} |\text{CCPF}_{y(\tau_n, t_m; \tilde{\mathbf{c}}_c)}(t_{\rho_i}; \Omega_i)|$;
end
 $\hat{\mathbf{\Omega}} = [\hat{\Omega}_1, \hat{\Omega}_2]^T$;
 $\mathbf{X} = \begin{bmatrix} 2 & 6t_{\rho_1} \\ 2 & 6t_{\rho_2} \end{bmatrix}$;
 $\hat{\mathbf{c}}'_f = \mathbf{X}^{-1}\hat{\mathbf{\Omega}}$;
return: $\hat{\mathbf{c}}'_f = [c'_{2,f}, c'_{3,f}]^T$.

Algorithm 2: DS-GIFT-CCPF

INPUT: Baseband signal $y(f_k, t_m)$ of the form (1) ;
OUTPUT: motion parameter estimates $\hat{\mathbf{c}}$;
Initialize $\hat{\mathbf{c}} = \emptyset$;
function DS-GIFT-CCPF ($y(f_k, t_m)$)
for $(\tilde{c}_{1,c}, \tilde{c}_{2,c}, \tilde{c}_{3,c}) \in \mathbb{C}_{1,c} \times \mathbb{C}_{2,c} \times \mathbb{C}_{3,c}$ **do**
 $\tilde{\mathbf{c}}_c := [\tilde{c}_{1,c}, \tilde{c}_{2,c}, \tilde{c}_{3,c}]^T$;
 $y(\tau_n, t_m; \tilde{\mathbf{c}}_c) := \text{mGIFT}(y(f_k, t_m), \tilde{\mathbf{c}}_c)$;
 for $\tau_n \in \frac{2c_0}{c} \tilde{\mathbb{C}}_0$ **do**
 $[\hat{c}'_{2,f}, \hat{c}'_{3,f}]^T := \text{CCPF}(y(\tau_n, t_m; \tilde{\mathbf{c}}_c))$;
 $\tilde{\mathbf{c}}'_f := [\hat{c}'_{1,f}, \hat{c}'_{2,f}, \hat{c}'_{3,f}]^T$;
 for $v_d \in \kappa \mathbb{C}_{1,f}$ **do**
 $y(\tau_n, v_d; \tilde{\mathbf{c}}'_{1,f}, \hat{c}'_{2,f}, \hat{c}'_{3,f}) := \text{GFT}_{y(\tau_n, t_m; \tilde{\mathbf{c}}_c)}(\tilde{\mathbf{c}}'_f)$;
 if $|y(\tau_n, v_d; \tilde{\mathbf{c}}'_{1,f}, \hat{c}'_{2,f}, \hat{c}'_{3,f})| > \gamma_{\text{LRT}}$ **then**
 $\hat{c}_0 := c\tau_n/2; \hat{c}_1 := \tilde{c}_{1,c} + v_d/\kappa; \hat{c}_2 := \tilde{c}_{2,c} + \hat{c}'_{2,f}/\kappa; \hat{c}_3 := \tilde{c}_{3,c} + \hat{c}'_{3,f}/\kappa$;
 $\hat{\mathbf{c}} := \hat{\mathbf{c}} \cup \{[\hat{c}_0, \hat{c}_1, \hat{c}_2, \hat{c}_3]^T\}$;
 end
 end
 end
end
return: $\hat{\mathbf{c}}$.

4.2. Computational Complexity Analysis

In what follows, the computational complexity (CC) of the DS-GIFT-CCPF detector is analyzed by comparison with the DS-GRFT, standard GRFT and ACCF-GFT detectors. Let M denote the number of pulses, N_0 the number of range bins, K the number of frequency bins (i.e., $K = N_0$), N_1 the number of velocity bins, N_2 the number of acceleration bins, N_3 the number of jerk bins and \tilde{N}_0 the number of range bins for the area of interest.

According to implementations of the four considered detectors, their computational costs are mainly due to four basic operations (BOs): matched filtering (MF), FFT, IFFT and CCPF(ACCF). Then, CC of these four basic operations and overall complexity for the different detectors are provided in Table 1. According to Table 1, the following conclusions can be drawn.

Table 1. Computational complexity of the GRFT, DS-GRFT and DS-GIFT-CCPF detectors.

Times Algs	BOs				Total CC
	MF $\mathcal{O}(M)$	IFFT $\mathcal{O}(0.5N_0 \log_2 N_0)$	CCPF $\mathcal{O}(2M)$ /ACCF $\mathcal{O}(N_0)$	FFT $\mathcal{O}(0.5M \log_2 M)$	
GRFT	$N_3 N_2 N_1 N_0$	$N_3 N_2 N_1 M$	–	–	$\mathcal{O}(MN_3 N_2 N_1 N_0 (1 + 0.5 \log_2 N_0))$
DS-GRFT	$\frac{f_s^2}{f_c^2} N_3 N_2 N_1 \tilde{N}_0$	$\frac{f_s^3}{f_c^3} N_3 N_2 N_1 M$	–	$\frac{f_s}{f_c} N_3 N_2 N_1 \tilde{N}_0$	$\mathcal{O}(\frac{f_s}{2f_c} MN_3 N_2 N_1 \tilde{N}_0 (\log_2 M + 2\frac{f_s}{f_c}) + \frac{f_s^3}{2f_c^3} MN_3 N_2 N_1 N_0 \log_2 N_0)$
DS-GIFT-CCPF	$\frac{f_s^3}{f_c^3} N_3 N_2 N_1 N_0 + 2\tilde{N}_0$	$\frac{f_s^3}{f_c^3} N_3 N_2 N_1 M$	$2\frac{f_s^3}{f_c^3} N_3 N_2 N_1 \tilde{N}_0 N_\Omega$	$\frac{f_s^3}{f_c^3} N_3 N_2 N_1 \tilde{N}_0$	$\mathcal{O}(2M\tilde{N}_0 + \frac{f_s^3}{2f_c^3} MN_3 N_2 N_1 N_0 (2 + \log_2 N_0) + \frac{f_s^3}{2f_c^3} MN_3 N_2 N_1 (8\tilde{N}_0 N_\Omega + \log_2 M))$
ACCF-GFT	$\frac{f_c}{f_s} \tilde{N}_0$	$M - 1$	$M - 1$	$\frac{f_c}{f_s} \tilde{N}_0$	$\mathcal{O}((M - 1)N_0 (1 + 0.5 \log_2 N_0) + \frac{f_c}{2f_s} M\tilde{N}_0 (2 + \log_2 M))$

First of all, the most computationally demanding part of the proposed DS-GIFT-CCPF is the CCPF operation. Furthermore, N_Ω can be considered to be comparable with the size of $\mathbb{C}_{2,f}$ or $\mathbb{C}_{3,f}$, i.e., $\frac{f_c}{f_s}$. As such, the CC of total CCPF operations becomes $8\frac{f_s^2}{f_c^2} MN_3 N_2 N_1 \tilde{N}_0$. Meanwhile, the FFT operation is the most computationally demanding part of DS-GRFT with the CC $\frac{f_s}{2f_c} MN_3 N_2 N_1 \tilde{N}_0 \log_2 M$. Thus, the CC of the DS-GIFT-CCPF is further reduced to about $\frac{8f_s}{f_c \log_2 M}$ of the DS-GRFT, since $\frac{f_s}{f_c}$ is generally a very small value and $\frac{8}{\log_2 M}$ is of the same order (say, when $M = 512$, $\frac{8}{\log_2 M} = 1$). Consequently, the DS-GIFT-CCPF has remarkable computational complexity reduction compared with the DS-GRFT.

Secondly, the most computationally demanding part of the standard GRFT is the MF operation. The CC of total MF operations is $MN_3 N_2 N_1 N_0$. Hence, the CC of the proposed DS-GIFT-CCPF is reduced to about $\frac{4f_s^2 \tilde{N}_0}{f_c^2 N_0}$ of the GRFT. Accordingly, the computational complexity of the DS-GIFT-CCPF is reduced significantly compared with the DS-GRFT.

Finally, for the ACCF-GFT detector, the most computationally demanding part is also the FFT operation, having the CC of $\frac{f_c}{2f_s} M\tilde{N}_0 \log_2 M$. Clearly, the computational complexity of the DS-GIFT-CCPF is about $\frac{16f_s^3 N_3 N_2 N_1}{f_c^3 \log_2 M}$ times that of the ACCF-GFT.

In general, the computational complexity of the proposed DS-GIFT-CCPF is higher than that of the ACCF-GFT but much lower than that of the GRFT and the DS-GRFT.

5. Performance Assessment

In this section, the proposed DS-GIFT-CCPF detector is assessed with respect to its coherent integration performance and computational efficiency, considering a scenario where both the transmitter and the receiver placed on the satellite observe high-speed, high-maneuvering targets. The radar cross-section of the targets is assumed to be of type Swerling 0. Experiments were carried out applying the bistatic radar geometry model of Figure 1 in Section 1. The parameters of the bistatic radar are summarized in Table 2.

Table 2. Parameter setting for the spatial-based bistatic radar system.

f_c [GHz]	f_s [MHz]	B_r [MHz]	PRF [Hz]	M
8	15.36	12.5	937.5	1024

5.1. Experiment 1

The purpose of this experiment was to show the effectiveness of the proposed DS-GIFT-CCPF in a challenging multi-target situation. We considered four moving targets with motion parameters as shown in Table 3. Specifically, to test performance of the proposed detector when dealing with targets that share similar kinematic characteristics and fall into the same range bin, we set motion parameters of targets to 1, 2 and 3. Furthermore, to test its applicability in dealing with well-separated targets, we set motion parameters of targets to 4.

Figure 2a–d show the range–pulse spectra at different stages of the RM correction. An obvious RM effect can be observed in Figure 2a. Figure 2b shows the range spectrum with slow time after coarse velocity compensation. It can be seen that the RM effect is partially corrected by 25 range bins for targets 1, 2 and 3. For target 4, according to Table 3, RMs caused by c_2 and c_3 could cancel each other out. Therefore, after coarse velocity compensation, RM is totally corrected for target 4. In Figure 2c, the result after coarse velocity and coarse acceleration compensation is given, showing that the RM effect has been corrected by 28 range bins for targets 1 and 2, 29 range bins for target 3 and 22 range bins for target 4. In Figure 2d, it is shown that, after coarse velocity, coarse acceleration and coarse jerk compensation, the RM effect has been eliminated. The aforementioned results demonstrate that the RM effect can be eliminated by coarse compensation alone. It should be noted that, for the sake of exhibition, the results in Figure 2a–d are given without noise background.

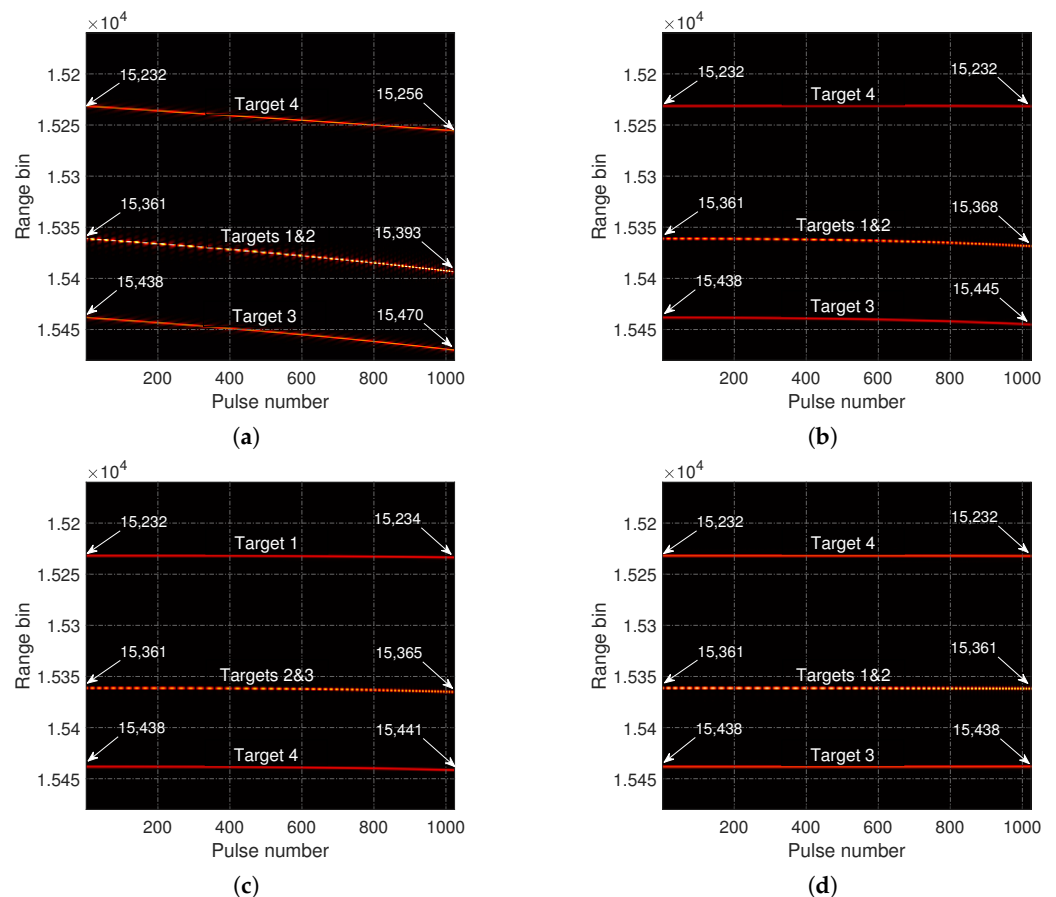


Figure 2. Range spectrum with slow time at different stages: (a) before RM correction; (b) after coarse acceleration compensation; (c) after RM compensation with respect to coarse acceleration and coarse velocity; (d) after RM compensation with respect to coarse jerk, coarse acceleration and coarse velocity.

Table 3. Motion parameters of multiple maneuvering targets in Experiment 1.

Num.	c_0 [km]	c_1 [m/s]	c_2 [m/s ²]	c_3 [m/s ³]	SNR after PC [dB]
target 1	150.00	225	29	28	−1.2
target 2	150.00	224	30	27	−1.8
target 3	150.75	225	27	25	−3.8
target 4	148.74	213	−10	12	−2.8

However, as Figure 3 shows, even if the RM effect has been eliminated, the target motion trajectory is submerged in the noise background due to the DFM effect.

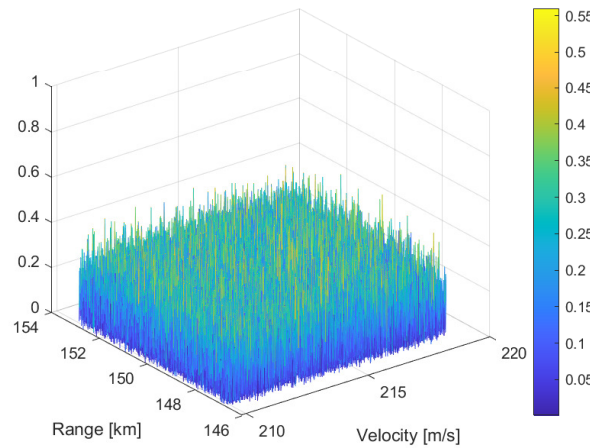
**Figure 3.** Range–Doppler spectrum after RM correction

Figure 4 illustrates the procedure of the DS-based estimation of target motion parameters. In particular, Figure 4 plots the maximum outputs of DS-GIFT-CCPF over slow time for each range bin. It can be observed that the peaks occur at range bins 15,232 (148.75 km), 15,361 (150.01 km) and 15,438 (150.76 km), which are consistent with the slant range values of the true objects. It should be noted that there are three peaks since targets 1 and 2 share the same range bin 15,361. Both targets 3 and 4 are located in different range bins than target 1. Without loss of generality, targets 1, 2 and 4 are considered in the following specific analysis of the procedure of the DS-GIFT-CCPF detector.

Figure 5a,d show the DS-based coarse motion parameter estimation procedure for targets 1, 2 and target 4. Specifically, Figure 5a shows the spectrum with respect to the coarse velocity, the coarse acceleration and the coarse jerk at range bin 15361 for targets 1 and 2. Observing Figure 5a, the maximum output is at coarse motion parameters (223.16, 28.59, 26.17). Then, at this maximum, we further plot the CCPF spectra in Figure 5b, from which it can be seen that $\hat{\Omega} \triangleq \begin{bmatrix} 6.77363 & 6.12902 \\ 5.54777 & 5.24892 \end{bmatrix}$. Additionally, $\mathbf{X} \triangleq \begin{bmatrix} 2 & 6t_{\rho_1} \\ 2 & 6t_{\rho_2} \end{bmatrix} \triangleq \begin{bmatrix} 2 & 0.5461 \\ 2 & 0.4864 \end{bmatrix}$.

Therefore, $\hat{\mathbf{c}}'_f = \mathbf{X}^{-1}\hat{\Omega} = \begin{bmatrix} 0.4400 & 1.7986 \\ 1.4077 & 0.8338 \end{bmatrix}^T$. The estimation of fine acceleration and fine jerk of targets 1 and 2 are (0.4403 m/s², 1.7980 m/s³) and (1.4088 m/s², 0.8345 m/s³), respectively. Then, it is shown in Figure 5c that both the RM and DFM are compensated on the basis of the estimated parameters in Figure 5a,b. According to results in Figure 5, by simple calculation according to (13), we can achieve the final parameter estimation results of target 1, which are $c_1 = 224.979$ m/s, $c_2 = 29.0303$ m/s² and $c_3 = 27.9680$ m/s³, while those of target 2 are $c_1 = 223.984$ m/s, $c_2 = 29.9988$ m/s² and $c_3 = 27.0045$ m/s³. Similar to Figure 5a,b, Figure 5d,e show the DS-based motion parameter estimation procedure for target 4. Finally, Figure 5f shows the range–Doppler spectrum after both RM and DFM are compensated for target 4. It can be seen that the target power is well-focused

after the compensation of target motion. The final estimated motion parameters of target 4 are $c_1 = 212.963$ m/s, $c_2 = -9.9328$ m/s² and $c_3 = 11.9561$ m/s³. Overall, the results are consistent with the parameters set in Table 3.

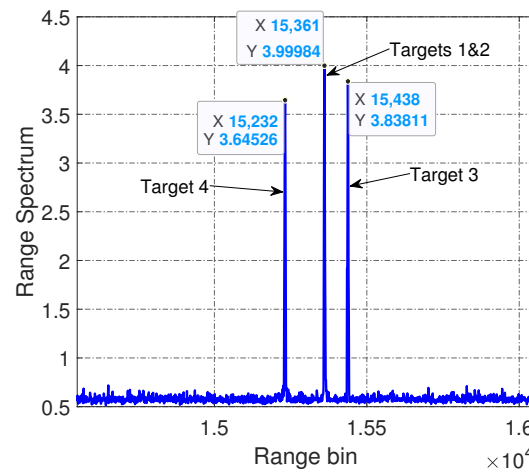


Figure 4. Maximum outputs of each range bin after RM and DFM corrections

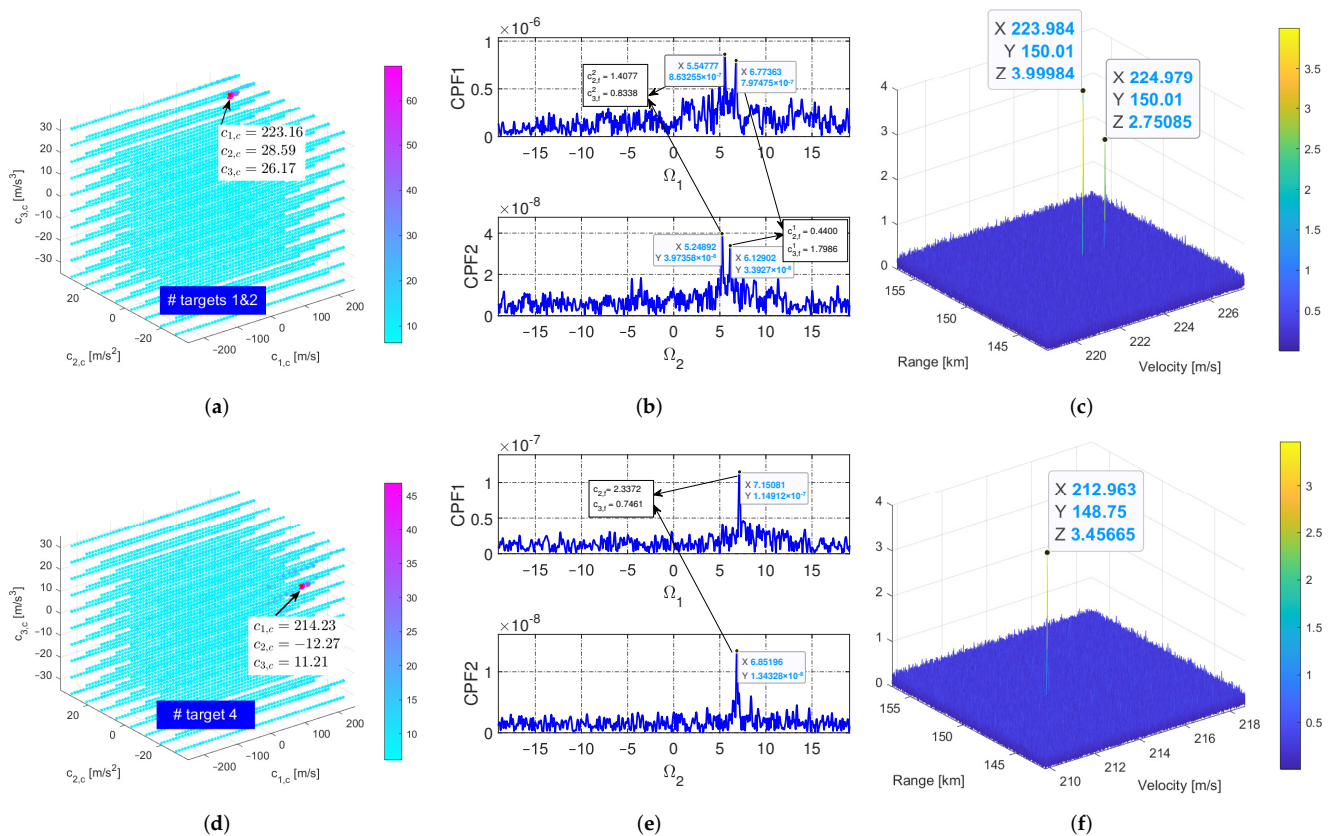


Figure 5. Estimation of target motion parameters: (a) coarse velocity, coarse acceleration and coarse jerk spectrum at range bin 15,361; (b) fine acceleration and fine jerk spectrum with estimated coarse motion parameters of (a); (c) range–Doppler spectrum after target motion compensation with estimated motion parameters of (a,b); (d) coarse velocity, coarse acceleration and coarse jerk spectrum at range bin 15,232; (e) fine acceleration and fine jerk spectrum with estimated coarse motion parameters of (c); (f) range–Doppler spectrum after target motion compensation with estimated motion parameters of (d,e).

Figure 6 further shows the Doppler spectra in the processing of fine motion parameter compensation. Figure 6a shows the DFM of targets 1 and 2 at range bin 15,361. In Figure 6b, the DFM has been partially compensated by fine acceleration but the energy is still dispersed. Figure 6c shows the Doppler spectrum after fine acceleration and fine jerk compensation of target 1. Finally, the fine velocity of target 1 is the velocity corresponding to the Doppler spectral peak. It is worth noting that there are two peaks in Figure 6c. The reason is that targets 1 and 2 share the same range bin and coarse motion parameters but the fine motion parameters are different. Compensating the fine motion parameters of target 1 is equivalent to partially compensating target 2, resulting the second extended peak in Figure 6c. Similarly, Figure 6d–f show the processing of fine motion parameters compensation of target 2. The second peak in Figure 6f expresses the energy extension of target 1. Figure 6g shows the Doppler spectrum of target 4 at range bin 15,232. Figure 6h shows the Doppler spectrum after compensating the fine acceleration. Then, it is shown in Figure 6i that the DFM is eliminated after compensating the fine acceleration and fine jerk.

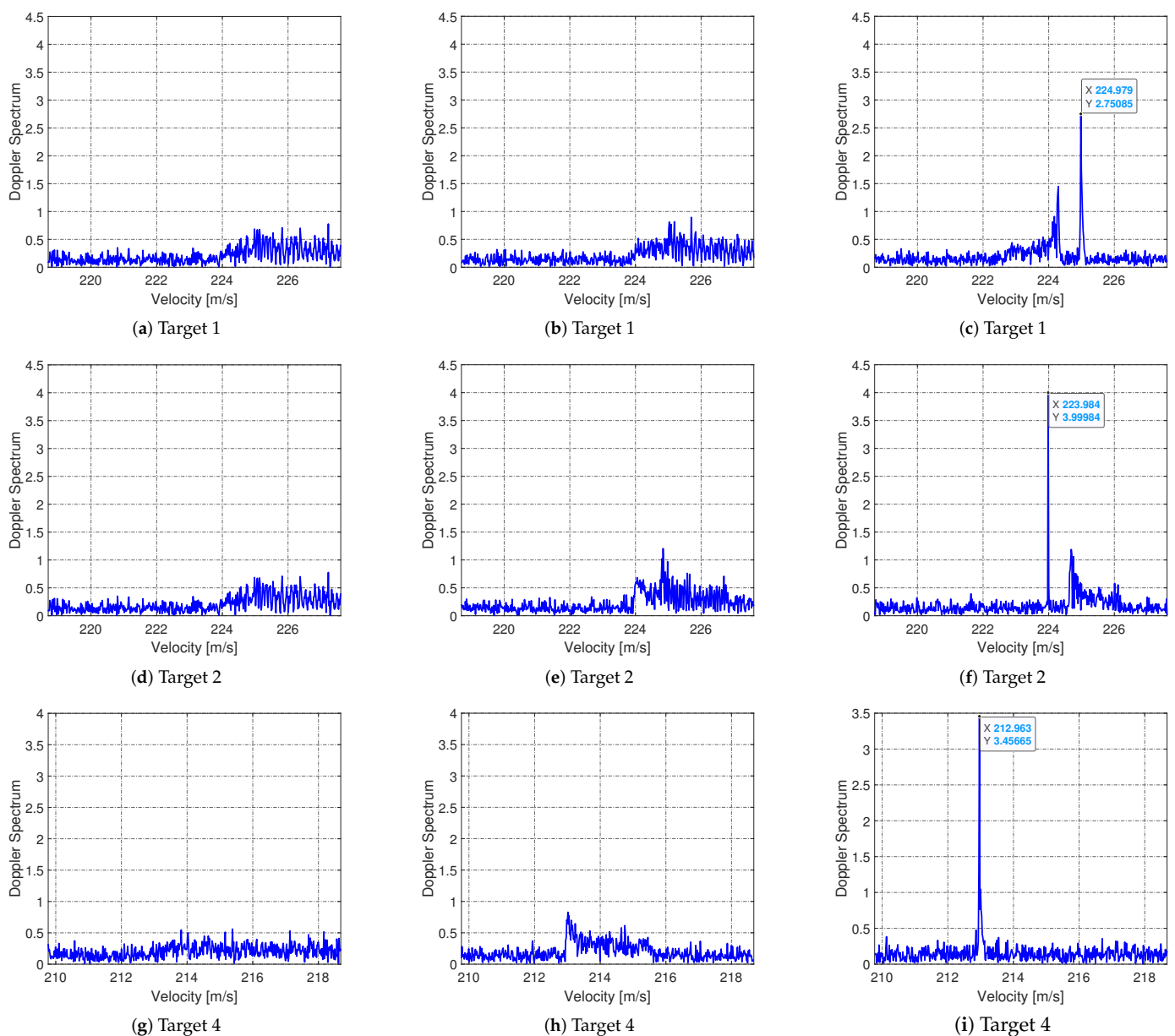


Figure 6. Doppler spectrum for targets 1, 2 and 4 at different stages: (a) after DFM compensation with respect to coarse motion parameters for target 1 at range bin 15,361; (b) after DFM compensation with

respect to coarse motion parameters and fine acceleration of target 1 at range bin 15,361; (c) after DFM compensation with respect to coarse motion parameters, fine acceleration and fine jerk of target 1 at range bin 15,361; (d) after DFM compensation with respect to coarse motion parameters of target 2 at range bin 15,361; (e) coarse motion parameters and fine acceleration of target 2 at range bin 15,361; (f) after DFM compensation with respect to coarse motion parameters, fine acceleration and fine jerk of target 2 at range bin 15,361; (g) after DFM compensation with respect to coarse motion parameters of target 4 at range bin 15,232; (h) after DFM compensation with respect to coarse motion parameters and fine acceleration of target 4 at range bin 15,232; (i) after DFM compensation with respect to coarse motion parameters, fine acceleration and fine jerk of target 4 at range bin 15,232.

5.2. Experiment 2

In this section, the performance of the proposed DS-GIFT-CCPF is assessed via 500 Monte Carlo runs. First, to provide a useful indicator for the step size of Ω , i.e., $\Delta\Omega$, we carried out different experiments under $|\overline{\mathbb{C}}_\Omega| = \{1270, 520, 400, 300, 260\}$ and the heterogeneous search space \mathbb{C}_Ω . Figure 7 shows the curves of detection performance for the proposed DS-GIFT-CCPF detector under the aforementioned settings. The dotted green line denotes that the probability of detection is 0.9. As expected, the proposed DS-GIFT-CCPF with the heterogeneous search space \mathbb{C}_Ω performs the best, while under the homogeneous search space, the detector performance degrades slightly as $|\overline{\mathbb{C}}_\Omega|$ decreases. Specifically, as observed from Figure 7, when $|\overline{\mathbb{C}}_\Omega|$ reaches the level of the fine motion parameter space, i.e., $|\overline{\mathbb{C}}_\Omega| = \frac{f_c}{f_s} = 520$, the performance loss can still remain at less than 1 dB. Considering this result, to balance the performance and the computational complexity, $|\overline{\mathbb{C}}_\Omega| = \frac{f_c}{f_s}$ can be a preferable choice in practice.

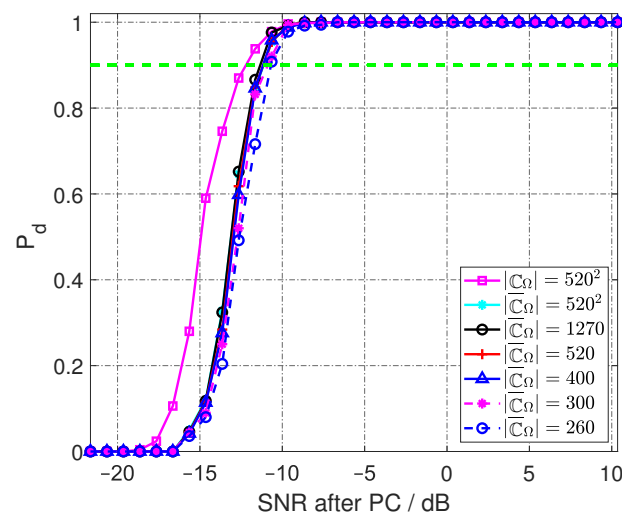


Figure 7. Detection probability versus pulse-compressed SNR for the proposed DS-GIFT-CCPF with different sizes of search space of Ω .

Then, the performance of the proposed DS-GIFT-CCPF detectors are further assessed by comparison with the standard GRFT [6], the DS-GRFT [15] and the ACCF-GFT [17,18] detectors considering the third motion parameters, as well as the DS-GRFT considering the second motion parameters [15]. Figure 8a shows the curves of detection performance for these five methods in different input SNR cases, and Figure 8b shows the theoretical complexity of the considered four methods for different values of f_c/f_s .

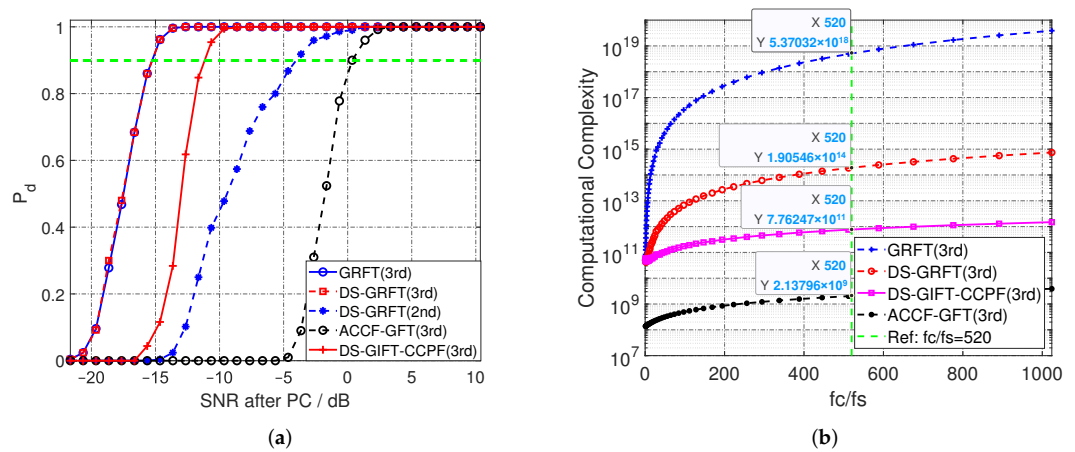


Figure 8. Performance comparison of different detectors: (a) detection probability versus pulse-compressed SNR; (b) computational complexity.

It can be seen from Figure 8a that, unsurprisingly, the DS-GRFT (third) has almost the same detection performance as the optimal GRFT detector. However, the DS-GRFT (second) detector is much worse than the DS-GRFT detector (third), with a 12 dB performance loss at $P_d = 0.9$, which is consistent with common sense. As for the ACCF-GFT detector, due to the high-order nonlinear operation and the error propagation effect, it performs even worse than the DS-GRFT (second). Specifically, it has a 15 dB performance loss at $P_d = 0.9$, also taking the DS-GRFT as the baseline. By contrast, the proposed DS-GIFT-CCPF detector only has about a 4 dB performance loss when $|\bar{C}_\Omega| = \frac{f_c}{f_s}$, compared to the DS-GRFT (third) detector at $P_d = 0.9$, demonstrating its ability when dealing with targets having high-order motions. On the other hand, as we can observe from Figure 8b, the computational complexity reduction of the DS-GIFT-CCPF detector relative to the DS-GRFT detector grows gradually as f_c/f_s increases. For the parameter setting of this experiment where $f_c/f_s = 520$, this reduction can reach more than two orders of magnitude, highlighting the computational efficiency of the proposed DS-GIFT-CCPF.

Table 4 further reports the execution time of different considered detectors at $f_c/f_s = 520$. Specifically, the velocity scope is set to 0–270 m/s, the acceleration scope to 0–40 m/s² and the jerk scope to 0–40 m/s³. Experiments were carried out in MATLAB 2023b using Intel Core i7-11700 with an eight-core 2.5-GHz CPU and 32 GB of RAM. It can be seen that the execution time of the DS-GIFT-CCPF is reduced by more than two orders of magnitude compared with the DS-GRFT, while it is reduced by seven orders of magnitude compared with the GRFT, further verifying the computational efficiency of the proposed detector.

To summarize, the above results demonstrate the computational efficiency of the proposed DS-GIFT-CCPF as well as a slight performance degradation relative to the DS-GRFT detector.

Table 4. Execution times of different detectors in Experiment 2.

Alg.s	GRFT	DS-GRFT	DS-GIFT-CCPF	ACCF-GFT
Execution Time [s]	1.78×10^{10}	5.09×10^4	2.48×10^2	3.16

6. Conclusions

To cope with the range migration (RM) and Doppler frequency migration (DFM) caused by high-order motion parameters for the space-based bistatic radar application, this paper proposed a computationally efficient long-time coherent integration (LTCI) method under the dual-scale (DS) motion parameter framework. First, the modified generalized inverse Fourier transform (GIFT) was performed on the coarse motion parameter space for

the RM compensation and a pre-compensation of DFM; a suitable designed conditioned cubic phase function (CCPF) was then proposed to estimate and compensate the fine part of high-order motion parameters conditioned on the coarse motion parameters, on the basis of which the GFT was finally used as the detection statistic to estimate all the motion parameters. The resulting LTCI algorithm is called the DS-GIFT-CCPF detector, which has shown a slight performance loss compared with the optimal GRFT (or DS-GRFT) detector, but achieved seven orders of magnitude of computational cost reduction with respect to the GRFT detector, and two orders of magnitude of computational cost reduction with respect to the DS-GRFT detector in numerical experiments.

Author Contributions: S.L., Project administration, Methodology, Formal analysis Supervision, Writing—review and editing; Y.W., Validation, Visualization, Resources, Writing—review and editing; Y.L., Resources, Writing—review and editing; B.W., Methodology, Writing—original draft and Conceptualization. All authors have read and agreed to the published version of the manuscript.

Funding: This work was supported by the National Natural Science Foundation of China (62301091, 62371078), Chinese Postdoctoral Science Foundation (2022M710533, 2022M710535), the Starting Research Fund from Chongqing University under Grant 02140011044134, Natural Science Foundation Project of Chongqing CSTB2022NSCQ-MSX1156.

Data Availability Statement: The research data is not public due to privacy.

Conflicts of Interest: The authors declare no conflict of interest.

Abbreviations

The following abbreviations are used in this paper:

f_k	the discrete frequency of the signal, $f_k = k\Delta f$
Δf	the interval of frequency bins
k	the number of frequency bins, $k = 1, \dots, K$
K	the number of frequency bins
t_m	the slow time (inter-pulse sampling time)
m	the number of pulses, $m = 1, \dots, M$
M	the number of pulses
f_c	the carrier frequency
c	the velocity of light
λ	the wave length
$R(t_m)$	the instantaneous slant range between the receiver and the transmitter
τ_n	the fast time (intra-pulse sampling time), $\tau_n = nT_s$
T_s	the sampling interval of fast time, $T_s = 1/f_s$
f_s	the sampling rate of frequency
B_r	the signal bandwidth, $B_r = K_{\text{valid}}\Delta f$
K_{valid}	the valid number of frequency bins
p	the order of the target motion parameters
c_0	the initial radial distance of the signal from the transmitter to the receiver
c_p	the radial components of the target of order p
\tilde{c}_p	the motion parameter variable of order p
$c_{p,\text{min}}$	the minimum value of \tilde{c}_p
$c_{p,\text{max}}$	the maximum value of \tilde{c}_p
$\tilde{c}_{p,c}$	the coarse motion parameter variable of \tilde{c}_p
$\tilde{c}_{p,f}$	the fine motion parameter variable of \tilde{c}_p
κ	the folding factor $\kappa \triangleq 1 - \frac{B_r}{2f_c}$
$\tilde{c}'_{p,f}$	the fine motion parameter variable of \tilde{c}_p weighted by κ
$\Delta c_{p,c}$	the step size of $\tilde{c}_{p,c}$
$\Delta c_{p,f}$	the step size of $\tilde{c}_{p,f}$
$c_{p,c}$	the coarse motion parameter of c_p
$c_{p,f}$	the fine motion parameter of c_p

$\hat{c}_{p,c}$	the estimation of $c_{p,c}$
$\hat{c}_{p,f}$	the estimation of $c_{p,f}$
$\hat{c}'_{p,f}$	the estimation of $c'_{p,f}$
$\mathbb{C}_{p,c}$	the search space of $\tilde{c}_{p,c}$
$\mathbb{C}_{p,f}$	the search space of $\tilde{c}_{p,f}$
$\mathbb{C}'_{p,f}$	the search space of $\tilde{c}'_{p,f}$
\mathbb{C}_f	the joint search spaces of the fine part of target motion parameters
\tilde{c}	the vector consisting of motion parameter variables
\tilde{c}_c	the vector consisting of coarse motion parameter variables
\tilde{c}_f	the vector consisting of fine motion parameter variables
\tilde{c}'_f	the vector consisting of fine motion parameter variables weighted by κ
c_c	the vector consisting of real coarse motion parameters
Ω	the constructed instantaneous frequency rate variable
\mathbb{C}_Ω	the search space of Ω
ρ_i	the i -th time position
$\overline{\mathbb{C}}_\Omega$	the homogeneous search space of Ω
$\hat{\Omega}$	the estimation of Ω
$\Delta\Omega$	the step size of $\overline{\mathbb{C}}_\Omega$
$ \cdot $	the size of the space
\hat{c}'_f	the vector consisting of $c'_{2,f}$ and $c'_{3,f}$
\hat{c}'_f	the estimation of \hat{c}'_f
\hat{c}_f	the vector consisting of $\hat{c}'_{2,f}$ and $\hat{c}'_{3,f}$
θ	the injective function from elements of Ω_1 to those of Ω_2

References

1. Wong, F.H.; Cumming, I.G.; Neo, Y.L. Focusing bistatic SAR data using the nonlinear chirp scaling algorithm. *IEEE Trans. Geosci. Remote Sens.* **2008**, *46*, 2493–2505. [\[CrossRef\]](#)
2. Ma, H.; Michail, A.; Debora, P.; Fabrizio, S.; Federica, P.; Marta, B.; Mikhail, C. Maritime moving target indication using passive GNSS-based bistatic radar. *IEEE Trans. Aerosp. Electron. Syst.* **2018**, *54*, 115–130. [\[CrossRef\]](#)
3. Feng, W.; Wei, W.; Liu, F. Modified keystone processing algorithm for the space-based bistatic radar systems. In Proceedings of the IET International Radar Conference 2015, Hangzhou, China, 14–16 October 2015; pp. 1–6.
4. Simpson, R. Spacecraft studies of planetary surfaces using bistatic radar. *IEEE Trans. Geosci. Remote Sens.* **1993**, *31*, 465–482. [\[CrossRef\]](#)
5. Zhang, J.; Ding, T.; Zhang, L. Long time coherent integration algorithm for high-speed maneuvering target detection using space-based bistatic radar. *IEEE Trans. Geosci. Remote Sens.* **2022**, *60*, 1–16.
6. Xu, J.; Xia, X.; Peng, S.; Yu, J.; Peng, Y.; Qian, L. Radar maneuvering target motion estimation based on generalized Radon-Fourier transform. *IEEE Trans. Signal Process.* **2012**, *60*, 6190–6201.
7. Chen, X.; Guan, J.; Liu, N.; He, Y. Maneuvering target detection via Radon-fractional Fourier transform-based long-time coherent integration. *IEEE Trans. Signal Process.* **2014**, *62*, 939–953. [\[CrossRef\]](#)
8. Xu, J.; Peng, Y.; Xiang, G. Radon-Fourier transform for radar target detection (III): optimality and fast implementations. *IEEE Trans. Aerosp. Electron. Syst.* **2012**, *60*, 6190–6201.
9. Xu, J. Radon-Fourier transform (RFT) for radar target detection I: generalized Doppler filter bank. *IEEE Trans. Aerosp. Electron. Syst.* **2011**, *47*, 1186–1202. [\[CrossRef\]](#)
10. Chen, X.; Guan, J.; Liu, N.; Zhou, W.; He, Y. Detection of a low observable sea-surface target with micromotion via Radon-linear canonical transform. *IEEE Geosci. Remote Sens. Lett.* **2014**, *60*, 6190–6210.
11. Li, X.; Cui, G.; Yi, W.; Kong, L. Coherent integration for maneuvering target detection based on Radon-Lv's distribution. *IEEE Signal Process. Lett.* **2015**, *22*, 1467–1471. [\[CrossRef\]](#)
12. Huang, P.; Liao, G.; Yang, Z.; Xia, X.G.; Ma, J.; Zheng, J. Long-time coherent integration for weak maneuvering target detection and high-order motion parameter estimation based on keystone transform. *IEEE Trans. Signal Process.* **2016**, *64*, 4013–4026. [\[CrossRef\]](#)
13. Sun, Z.; Li, X.; Yi, W.; Cui, G.; Kong, L. Detection of weak maneuvering target based on keystone transform and matched filtering process. *Signal Process.* **2017**, *140*, 127–138. [\[CrossRef\]](#)
14. Li, Y.; Zeng, T.; long, T.; Wang, Z. Range migration compensation and Doppler ambiguity resolution by keystone transform. In Proceedings of the 2006 CIE International Conference on Radar (CIE ICR), Shanghai, China, 16–19 October 2006; pp. 1–4.
15. Li, S.; Wang, Y.; Wang, B.; Battistelli, G.; Chisci, L.; Cui, G. Efficient dual-scale generalized Radon-Fourier transform detector family for long time coherent integration. *arXiv* **2024**, arXiv:2403.06788. <https://doi.org/10.48550/arXiv.2403.06788>.

16. Huang, P.; Liao, G.; Yang, Z.; Xia, X.; Ma, J. Ground maneuvering target imaging and high-order motion parameter estimation based on second-order keystone and generalized Hough-HAF transform. *IEEE Trans. Geosci. Remote Sens.* **2017**, *55*, 320–335. [[CrossRef](#)]
17. Li, X.; Cui, G.; Yi, W.; Kong, L. A fast maneuvering target motion parameters estimation algorithm based on ACCF. *IEEE Signal Process Lett.* **2015**, *22*, 270–274. [[CrossRef](#)]
18. Yu, L.; He, F.; Zhang, Q.; Su, Y.; Zhao, Y. High maneuvering target long-time coherent integration and motion parameters estimation based on Bayesian compressive sensing. *IEEE Trans. Aerosp. Electron. Syst.* **2023**, *59*, 4984–4999. [[CrossRef](#)]
19. Wang, B.; Li, S.; Battistelli, G.; Chisci, L. Dual-scale generalized Radon-Fourier transform family for long time coherent integration. In Proceedings of the 11th International Conference on Control, Automation and Information Sciences (ICCAIS), Hanoi, Vietnam, 21–24 November 2022; pp. 499–505.
20. Key, E.L.; Fowle, E.N.; Haggarty, R.D. A method of designing signals of large time-bandwidth product. *IRE Int. Conv. Rec.* **1961**, *4*, 146–154.
21. Smith, J.O. Spectral Audio Signal Processing. Available online: <http://books.w3k.org/> (accessed on 12 March 2024).
22. Wang, B.; Li, S.; Battistelli, G.; Chisci, L. Fast iterative adaptive approach for indoor localization with distributed 5G small cells. *IEEE Wirel. Commun. Lett.* **2022**, *11*, 1980–1984. [[CrossRef](#)]
23. Fessler, J.; Sutton, B. Nonuniform fast Fourier transforms using minmax interpolation. *IEEE Trans. Signal Process.* **2003**, *51*, 560–574. [[CrossRef](#)]
24. O’Shea, P. A fast algorithm for estimating the parameters of a quadratic FM signal. *IEEE Trans. Signal Process.* **2004**, *52*, 385–393. [[CrossRef](#)]
25. Lv, Y.; Wu, Y.; Wang, H.; Qiu, L.; Jiang, J.; Sun, Y. An inverse synthetic aperture ladar imaging algorithm of maneuvering target based on integral cubic phase function-fractional Fourier transform. *Electronics* **2018**, *7*, 148. [[CrossRef](#)]
26. Wang, P.; Yang, J. Multicomponent chirp signals analysis using product cubic phase function. *Digit. Signal Process.* **2006**, *16*, 654–669. [[CrossRef](#)]
27. Zhang, J.; Su, T.; Zheng, J.; He, X. Parameter estimation of CFM signals based on MICPF-HAF. *Electron. Lett.* **2018**, *54*, 456–458. [[CrossRef](#)]
28. Vo, B.N.; Vo, B.T.; Phung, D. Labeled Random finite sets and the Bayes multi-target tracking filter. *IEEE Trans. Signal Process.* **2014**, *62*, 6554–6567. [[CrossRef](#)]

Disclaimer/Publisher’s Note: The statements, opinions and data contained in all publications are solely those of the individual author(s) and contributor(s) and not of MDPI and/or the editor(s). MDPI and/or the editor(s) disclaim responsibility for any injury to people or property resulting from any ideas, methods, instructions or products referred to in the content.